Surface Morphologies in Ultra-short Pulsed Laser Processing of Stainless-Steel at High Repetition Rate

G. Lazzini, L. Gemini, A. H. A. Lutey, R. Kling, L. Romoli, M. Allegrini & F. Fuso

International Journal of Precision Engineering and Manufacturing

ISSN 2234-7593

Int. J. Precis. Eng. Manuf.
DOI 10.1007/s12541-019-00174-1

International Journal of Precision Engineering and Manufacturing
https://doi.org/10.1007/s12541-019-00174-1

Online ISSN 2005-4602
Print ISSN 2234-7593

REGULAR PAPER

Surface Morphologies in Ultra-short Pulsed Laser Processing of Stainless-Steel at High Repetition Rate

G. Lazzini[1] · L. Gemini[2] · A. H. A. Lutey[1] · R. Kling[2] · L. Romoli[1] · M. Allegrini[3] · F. Fuso[3,4]

Received: 9 August 2018 / Revised: 11 June 2019 / Accepted: 12 June 2019

Abstract

Stainless-steel is ablated with femtosecond laser pulses at high repetition rate. A multi-pass, high spatial overlap laser scanning strategy is applied in order to cope with the requirements for large-scale machining of high aspect ratio structures. Topography of the processed surfaces is analyzed via Shear Force Microscopy scans, with the main aim to investigate morphology changes as a function of process parameters. Quantitative assessment of local height variations enables a detailed investigation of the produced features. Depending on the process parameters, in particular on laser fluence and repetition rate, a transition from small islands to large bumps is observed, explained in terms of feature coalescence.

Keywords Nanostructured surfaces · Laser machining · Shear force microscopy · Directed energy surface treatments

List of symbols

X	Longitudinal direction of laser scan
Y	Lateral direction of laser scan
RR	Laser repetition rate
v	Laser scan speed
F	Laser fluence
S_q	Root-mean-square roughness
S_{pd}	Surface peak density according to ISO 12178
A_{ma}	Average motif area according to ISO 12178
S_{ks}	Motif mean slope according to ISO 12178

✉ F. Fuso
francesco.fuso@unipi.it

G. Lazzini
gianmarco.lazzini@unipr.it

L. Gemini
laura.gemini@alphanov.com

A. H. A. Lutey
adrianhughalexander.lutey@unipr.it

R. Kling
rainer.kling@alphanov.com

L. Romoli
luca.romoli@unipr.it

M. Allegrini
maria.allegrini@unipi.it

1 Department of Engineering and Architecture, University of Parma, 43124 Parma, Italy

2 ALPhANOV, Institut d'Optique d'Aquitaine, 33400 Talence, France

3 Dipartimento di Fisica Enrico Fermi, Università di Pisa, 56127 Pisa, Italy

4 Istituto Nazionale di Ottica, INO-CNR, 56124 Pisa, Italy

1 Introduction

Directed energy processing techniques are amongst the most efficient for producing tailored surface property modifications [1]. Engineered surfaces, in particular those exhibiting micro- and nano-scale patterns, are presently receiving much attention due to the wide variety of advanced applications in which they can be employed. For instance, creation of biomimetic surfaces [2, 3] holds much promise for substantial advancements in the field of bio interfaces by controlling wetting properties [4, 5] and preventing bio-film growth [6, 7].

Many techniques can be used to produce patterned surfaces, including optical lithography [8], nano-imprinting of soft matter [9], electron beam lithography [10, 11], ion beam sputtering [12, 13]. Large-scale fabrication of biomimetic surfaces, however, relies on the ability to up-scale a given technology in order to achieve high throughput at a reasonable cost, which is not always ensured by the aforementioned methods. Directed energy techniques based on pulsed lasers [14] represent an appealing alternative thanks to their versatility, minimal invasiveness, absence of sample preparation requirements and possibility of being performed in air.

Published online: 20 June 2019

The high repetition rate of current state-of-the-art ultra-short pulsed laser sources enables the deployment of processing strategies that achieve high throughput at a large scale. In contrast to longer laser pulses, interaction with sub-picosecond pulses produces a very limited Heat Affected Zone (HAZ) in the target [15], leading to negligible material recast and to spatially well-defined surface modifications. In addition, self-organization processes in metastable and highly energetic ablated layers can produce quasi-periodic nanostructures known as Laser Induced Periodic Surface Structures (LIPSS) [16, 17]. Repetitive laser irradiation of a solid surface, however, creates a complicated scenario where many physical mechanisms take place simultaneously.

This paper presents an experiment where AISI 316L stainless-steel, a material used in many industrial applications, is ablated with 350 fs laser pulses of wavelength 1030 nm. Process parameters, including laser fluence, repetition rate, scanning speed, are varied over a wide range of values and the resulting surface features are analyzed with the main aim of identifying the role played by each parameter.

The investigated samples are similar to those reported in a previous paper [18], where applicability within the framework of bio-film prevention was discussed on the basis of optical profilometry and electron microscopy data. In the present work, sample surfaces are studied through three-dimensional topographic maps with a spatial resolution in the range of a few tens of nanometers, or better. Shear Force Microscopy (ShFM) [19], a variant of Scanning Probe Microscopy (SPM) specifically conceived for topographic analysis at the sub-micrometer scale, is employed. Choice of this experimental technique is motivated by its proven ability to measure the height of the surface features, further to reconstruct their shape and transverse size as with other diagnostics (e.g., optical and electron microscopes). This enables quantitative determination of areal surface parameters relevant to characterization of the process. It is found that different ablation regimes can take place featuring dense arrays of small islands or micrometer-sized bumps, depending on both laser fluence and repetition rate.

2 Experimental

Ablation is performed on $50 \times 50 \times 2$ mm^3 AISI 316L stainless-steel plates mirror polished and ultrasonically cleaned in acetone at room temperature. The choice of material is motivated by the widespread use of AISI 316L in industrial contexts such as food handling, precision mechanics, medical implants and marine applications.

Laser irradiation is carried out with an Amplitude Systems Satsuma HP3 laser source emitting linearly polarized pulses of duration 350 fs and wavelength $\lambda = 1030$ nm, capable of an average power up to 40 W and a repetition rate up to 1 MHz. A galvanometric head is employed to move the focused spot on the surface and perform parallel-line laser scanning over an 8×8 mm^2 area, as sketched in Fig. 1. The scanning strategy is designed to maintain constant pulse spatial overlap along the longitudinal (*X*) and lateral (*Y*) directions of 92% and 80% of the laser spot diameter, respectively. Four distinct combinations of RR and v are chosen, see Table 1, in order to achieve a longitudinal pulse spacing of 2 µm, whereas the lateral hatch is set to 5 µm. Samples have been produced with six values of laser fluence, in the nominal range 0.36–1.35 J/cm^2, with $N_p = 10$ laser passes performed over the entire machined area. A total number of 64×10^6 laser pulses is therefore delivered to the sample, independent of the processing parameters employed.

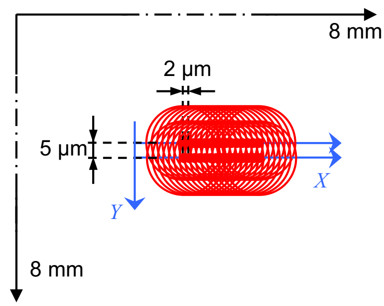

Fig. 1 Sketch of the scanning strategy: the laser spot, indicated by red circles of diameter 25 µm, is displaced after every laser pulse by 2 µm in the longitudinal direction (*X*). After one line is processed, the spot is laterally displaced by a hatch spacing of 5 µm along *Y*. The whole process is repeated 10 times, leading to deliver a total number of 64×10^6 laser pulses to the sample

Table 1 Laser repetition rate (RR), scan velocity (v) and fluence (F) used in the experiment. The total processing time resulting from the combination of RR and v is also reported

RR [kHz]	v [cm/s]	Processing time [s]
1000	200	64
500	100	128
250	50	256
100	20	640

F [J/cm^2]
0.36
0.48
0.69
0.86
1.14
1.35

The ShFM technique [19–21] used to investigate the machined samples employs a metal tip consisting of an electrochemically-etched tungsten wire (0.125 mm diameter). The etching procedure, using KOH and controlled AC-current [19], leads to a typical tip diameter of around 50 nm and an apical half-angle below 12°, confirmed via electron microscope imaging of several probes. The tip is glued to the prong of a quartz tuning-fork, maintained in dithering oscillation parallel to the sample surface by a piezoelectric actuator. The oscillation frequency is set close to the mechanical resonance of the system (around 32 kHz), with the amplitude continuously monitored via the signal produced by the tuning fork.

The oscillation is strongly damped when the tip-to-surface distance decreases below a few nm due to shear forces resulting mostly from friction in the air layer trapped between the tip and the surface [22]. The oscillation amplitude signal can therefore be used in a feedback configuration to maintain constant-gap operation during the scan. As with all SPM techniques, this leads to topographic maps of the surface, which, owing to the sensing mechanism involved, are acquired in true non-contact mode. Part of the tuning fork signal is sent into a digital dual lock-in amplifier (Stanford Research Systems SR830DSP) synchronous with the dithering oscillation, whose amplitude and phase outputs are continuously acquired during every scan. The phase difference between sinusoidal driving signal and actual tip oscillation is extremely sensitive to small variations in tip-to-sample distance, leading to detect small topographical features and their borders.

The ShFM setup is based on a RHK SPM-100 controller and a Physik Instrumente P-517.3 3-axis piezoelectric nanopositioner, enabling sample scanning with a maximum travel of 100 µm in the two horizontal directions under closed-loop operation and 20 µm along the vertical direction, used to adjust the tip-to-sample distance. Positioning accuracy is 1 nm and 0.1 nm in the horizontal and vertical directions, respectively. The *X*- and *Y*-directions of the ShFM maps are chosen so as to correspond with the respective directions of laser scanning within a ± 5° accuracy. Prior to analyzing the machined regions, reference scans of the flat, non-machined, surface are carried out and residual slopes carefully compensated for down to a few mrad. Unless otherwise stated, topographic maps consist of raw (unfiltered) data. Several maps are acquired on different areas of each sample to check repeatability, and representative examples are presented.

3 Results and Discussion

The depth of the laser ablated region is evaluated by scanning areas close to the edge of the laser irradiated surface, in order to directly reveal the vertical distance between non-machined and machined areas. Results are summarized in Fig. 2 as a function of the laser fluence for all tested combinations of RR and v. Markers show the average vertical distance, in absolute value, between the reference surface and the average plane of the machined surface, while reported error bars display minimum and maximum measured values. Measurement uncertainty is considered negligible with respect to the variation of the measured values.

On average, an ablation depth slightly above 10 µm is found. Taking into account machined area and total number

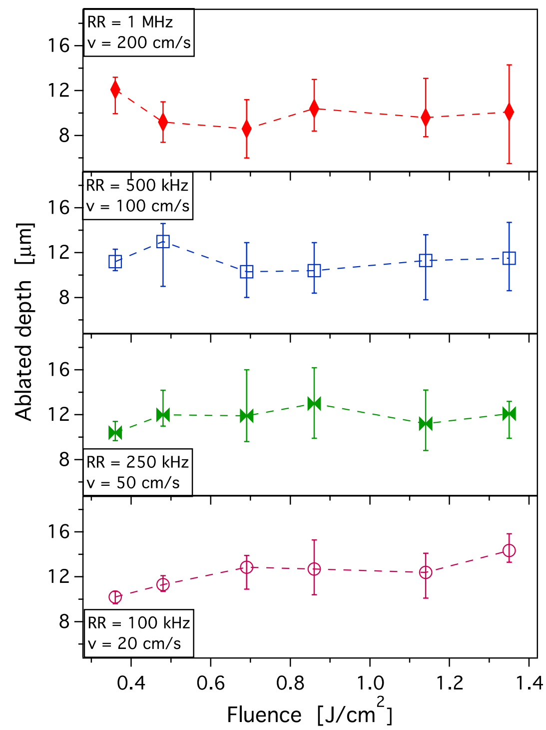

Fig. 2 Ablated depth as a function of laser fluence for different combinations of RR and v. Dashed lines are guides for the eye

of laser pulses, we can estimate an ablated volume around 10 µm^3 per pulse, corresponding to an average ablation depth of approximately 20 nm per pulse. The obtained value is in rough agreement with published data [23] for 316L stainless-steel using a Ti:Sa fs-laser at a fluence of approximately 0.2 J/cm^2. With ultra-short pulsed lasers, the ablation depth is known to follow a sub-linear behavior with fluence [24]. In our experiment no clear relationship between ablation depth and laser fluence can be observed, in particular for samples machined at high repetition rates, indicating non-trivial interplay between different phenomena, including partial redeposition of ablated material and absorption of laser energy by ablated products.

3.1 Morphology at Low Fluence

Laser machining obviously leads to rough surfaces showing distinctive features denoted here as islands, which appear in the topography as hills with well-defined borders. At low laser fluence, a rather homogenous texture of relatively small islands is observed via ShFM scans, featuring an anisotropic, ellipsoidal shape. For instance, Fig. 3a shows a topographic map of a sample machined at RR = 1 MHz and the minimum fluence explored in the present experiment, F = 0.36 J/cm^2, relatively close to the ablation threshold of 0.13 J/cm^2 reported for Ti:Sa fs-laser ablation of 316L stainless-steel [23].

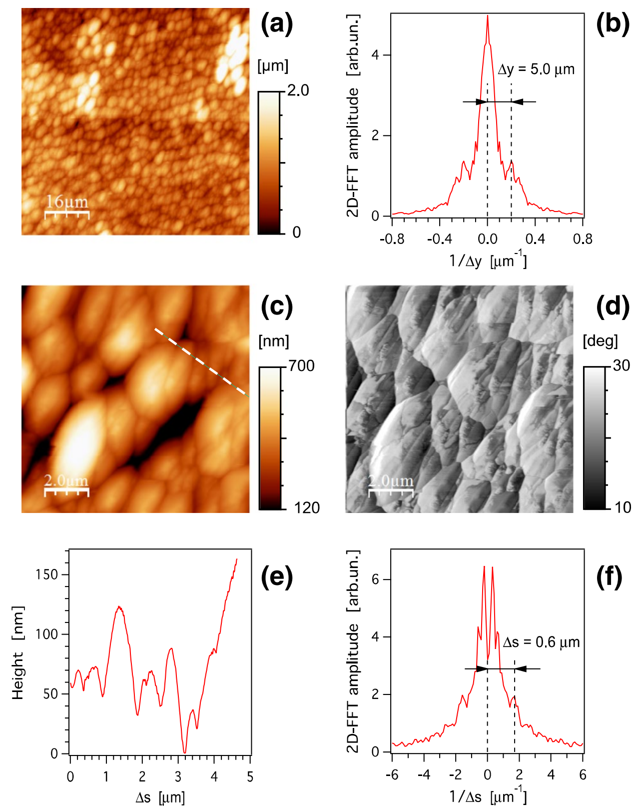

Fig. 3 Maps and data acquired via ShFM scans on a sample processed at F = 0.36 J/cm^2, RR = 1 MHz and v = 200 cm/s: 80 × 80 µm^2 topographic map (**a**) and line-profile of the corresponding 2D-FFT map (**b**) in the *Y*-direction; 10 × 10 µm^2 topographic (**c**) and phase (**d**) maps; line-profile of the topography (**e**) and of the 2D-FFT map (**f**) along the dashed segment superposed to the map in (**c**)

Periodicities in the topography can be assessed by two-dimensional Fast Fourier Transform (2D-FFT) analysis. A line-profile of the 2D-FFT map along the *Y*-direction, computed using the open-source Gwyddion software [25], is given as an example in Fig. 3b. The horizontal axis of the plot reports the inverse spacing in the *Y*-direction of the map in Fig. 3a, denoted here as $1/\Delta y$ with units of µm^{-1}, whereas the vertical axis is calibrated in arbitrary units of 2D-FFT amplitude. A peak can be clearly observed at a spacing corresponding to $\Delta y \sim 5$ µm. Such a finding is common to all scans carried out on samples machined at F = 0.36 J/cm^2, independent of the scanned region within the processed area or combination of RR and v. Other smaller peaks can also be seen, indicating residual waviness of the machined substrate with a spacing of 20–30 µm, and additional periodicities at short-scale, corresponding to $\Delta y < 5$ µm. The prominent periodicity can be directly related to the lateral hatch spacing of the laser processing scan, set to the nominal value of 5 µm. Therefore, we can conclude that island anisotropy in low-fluence ablation is dominated by the geometric anisotropy of the process.

Local morphology can be better assessed by analyzing scans performed over smaller areas such as 10 × 10 µm^2 due to the higher in-plane measurement resolution. An example is given in Fig. 3c, d, reporting topographic and phase maps, respectively, of a portion of the same sample as in Fig. 2a. Island morphology is very clear, with elongated shapes featuring lengths and widths in the order of 4–5 µm and 2–3 µm, respectively. Island height is typically in the order of several hundreds of nanometers. The phase map presented in Fig. 3d enables detecting the presence of tiny elongated features, oriented approximately 20°–25° to the *Y*-direction and well-aligned with each other. Such features, clearly visible in almost all of the scanned area, can be interpreted as LIPSS. The onset and causes of LIPSS have been discussed extensively in the literature. Following on from the ideas originally proposed by Sipe and coworkers [26, 27] in 1983, most theoretical interpretations of LIPSS on metals involve interference between the incident laser radiation and surface waves that develop due to collective oscillation of the surface free charge. The periodicity of the so-produced nanostructures, known as Low Spatial Frequency LIPSS (LSFL) [16, 28], depends on the laser wavelength λ as well as other process parameters, including the angle of incidence, and is generally found in the range $\lambda/2 - \lambda$.

The mechanisms underlying LIPSS formation become more complicated under processing conditions involving pulse overlap and multi-pass machining strategies. Interaction of a laser pulse with a surface that has already been irradiated can be affected, for instance, by the presence of previously inscribed nanostructures as well as the occurrence of surface slopes [20, 29, 30]. Nonetheless, LIPSS are reported on various substrates even with complex laser processing strategies aimed at texturing large size surfaces [31–34].

LIPSS found on our samples processed at low fluence are associated with small height variations. Figure 3e reports a line-profile analysis drawn along the dashed segment superposed to the map in Fig. 3c, where the occurrence of grooves, a few tens of nanometers deep, can be observed separating adjacent LIPSS. Figure 3f shows a line-profile drawn along the same segment on the 2D-FFT of the map in Fig. 3d. The most prominent peak corresponds to a periodicity $\Delta s \sim 0.6$ µm, slightly larger than half the laser wavelength, therefore in agreement with standard LSFL structures. LIPSS orientation for linearly polarized laser beams is expected [16] orthogonal to the polarization direction. In our experimental configuration, LIPSS should be aligned with the *Y*-direction of the ShFM scan within the ± 5° accuracy mentioned in Sect. 2. The observed misalignment with respect to the expectations can be ascribed to deviations of the actual polarization direction in the laser focal spot and to modifications of the laser/matter interaction processes

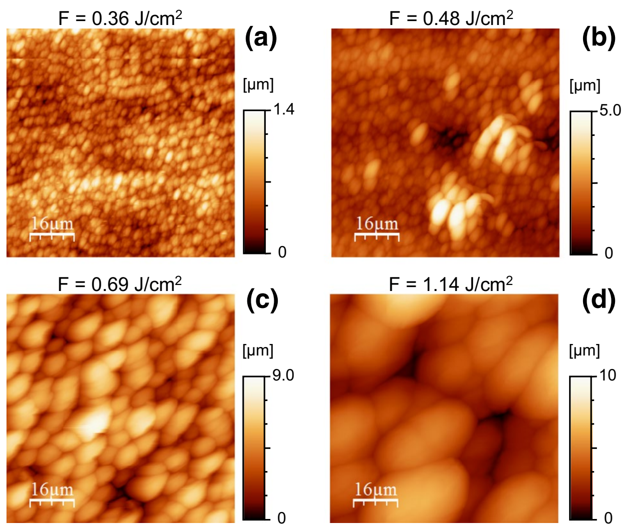

Fig. 4 80 × 80 μm^2 topographic maps of samples processed at RR = 500 kHz, v = 100 cm/s and increasing fluence (**a**)–(**d**)

consequent to the arrival of laser pulses onto already roughened surfaces [19, 20, 30].

3.2 Morphology at Moderate and High Fluence

By increasing the fluence well above the ablation threshold, markedly different morphologies are observed. Figure 4 shows 80 × 80 μm^2 topographic maps acquired with increasing fluence for samples processed at RR = 500 kHz. Fluence increase leads to higher islands whose morphology is similar to large surface bumps starting from F = 0.48 J/cm^2. At the maximum fluence explored in the present experiment, bumps with a transverse size in the order of 20–30 μm are found, with asymmetrical shapes featuring a long axis oriented 30°–45° with respect to the *Y*-direction.

The aspect ratio of the islands, defined as the ratio of height to transverse size, is maximum at the intermediate regime corresponding to moderate fluence. Bumps occurring at F = 0.69 J/cm^2, for instance, show a relatively homogeneous transverse size of 6–10 μm over the entire ShFM scanned region, while height is in the range 4–7 μm, yielding an average aspect ratio above 0.7. For comparison, the homogeneous texture of small islands occurring at low fluence exhibits a typical aspect ratio well below 0.5. Moreover, the increase in transverse size at higher fluence is not accompanied by a corresponding increase in height, resulting again in an aspect ratio below 0.5. Similar morphologies have been reported [35] in 316L stainless-steel irradiated with 490 fs laser pulses at a wavelength of 1043 nm using a large number of subsequent scans, N_p up to several thousands. Such a specific processing strategy led to a dense texture of high aspect ratio microstructures, identified as conical micro-spikes [35–37] and interpreted on the basis of two distinct processes: (i) interplay between ablation and partial redeposition of material, and (ii) a comparatively smaller ablation rate on inclined surfaces due to a lower effective fluence as the laser spot is projected over a larger surface area. It has been proposed that this can inhibit ablation in some regions at low fluence, leading to prevalence of redeposition over ablation [35]. At higher fluence, material removal takes place over the entire surface, including inclined areas, leading to conical micro-spikes with a spacing dictated by the hatch spacing of the laser scan.

In the present experiment a smaller number of laser passes (N_p = 10) is used. As a consequence, spacing and morphology of the produced bumps are not dictated by the hatch spacing. Instead, phenomena involving melt hydrodynamics complemented with electromagnetic interference [38] play a role in governing the transition from small islands to large bumps and in ruling their geometry.

Analysis of small features superimposed on the bumps, such as those shown in Fig. 5 for a sample processed at F = 0.69 J/cm^2 and RR = 500 kHz, reveals the occurrence of aligned grooves oriented approximately at 50° to the *Y*-direction. Such grooves, a few tens of nanometers deep, can again be related to LIPSS. Their typical spacing, however, corresponds to periodicities also below half the laser wavelength, in the order of λ/3 and λ/4. Both spacing and orientation demonstrate the occurrence of another class of LIPSS, known in the literature [16] as High Spatial Frequency LIPSS (HSFL) and expected to be oriented along the polarization direction.

3.3 Areal Surface Parameters

Qualitative observations of topographic maps reported so far highlight the role of laser fluence in driving a transition from small islands to large bumps. Modifications in surface morphology can be assessed for the whole set of investigated samples by analyzing several selected areal surface parameters, reliably evaluated thanks to the accurate ShFM

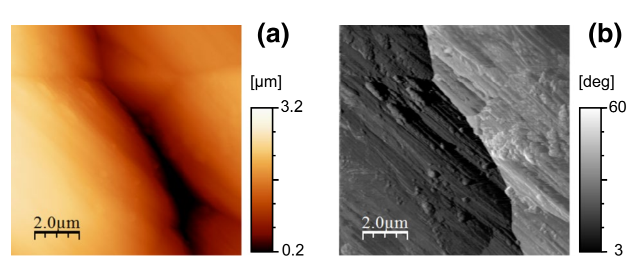

Fig. 5 10 × 10 μm^2 topographic (**a**) and phase (**b**) maps of a sample processed at F = 0.69 J/cm^2, RR = 500 kHz and v = 100 cm/s. Note that the different average level in the left and right portions of (**b**) reflects the occurrence of negative and positive topographic slopes during the scan, corresponding to a decrease and increase in the measured phase difference, respectively

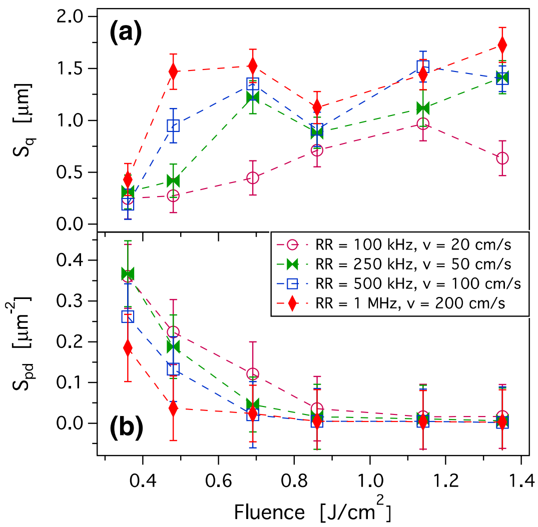

Fig. 6 RMS roughness S_q (**a**) and density of peaks S_{pd} (**b**) as a function of the laser fluence for different combinations of RR and v, as in legend. Data are evaluated averaging over several 80 × 80 µm^2 topographic maps; standard deviation is used for error bars. Dashed lines are guides for the eye

topographic mapping. Figure 6a reports the root-mean-square surface roughness (S_q) as a function of F. In principle, roughness is expected to increase with fluence owing to increased ablation rate. Data shown in Fig. 2 demonstrate, however, that the ablated depth follows a non-monotonic trend, except for the combination of RR = 100 kHz and v = 20 cm/s. This is reflected in the behavior of S_q, where an increasing trend is suggested only for this choice of RR and v. Other combinations lead to a local minimum in S_q at F = 0.86 J/cm^2, demonstrating that the transition from small islands to large bumps occurs around such a fluence value.

A specific parameter useful for assessing morphology is the density of peaks (S_{pd}), defined as the number of peaks per unit area. This parameter is calculated within the framework of ISO 12178 standard [39] utilizing an algorithm implemented in Python code and based on so-called watershed segmentation, where local surface hills, or motifs, are distinguished or segmented. The standard also requires application of so-called Wolf pruning, an algorithm that excludes motifs whose height falls below a certain threshold. Wolf pruning becomes meaningful for peaks whose heights are distributed over a large interval of values, which is not our case (see, e.g., Fig. 3e).

The behavior of S_{pd} as a function of F, shown in Fig. 5b, confirms previously noted qualitative observations. At low F, increasing fluence leads to a growth in peak size and therefore a reduction in their density. With a further increase S_{pd} tends to an asymptotic value above F = 0.86 J/cm^2, where the local minimum in S_q is observed, independent of the RR and v combination.

This finding is a signature of the coalescence process where neighboring small islands merge each other giving rise to larger features, eventually leading to large bumps. To confirm this hypothesis, two additional areal parameters are calculated, the motif average area and motif mean slope.

The motif average area (A_{ma}), defined as the arithmetic mean area of all motifs, is reported in Fig. 7a as a function of the laser fluence. Data exhibit an almost monotonic increase with F, being the growth rate less pronounced at low RR. This behavior reflects the previously described increase in transverse size of bumps (see, for instance, Fig. 4). While S_{pd}, measured on 80 × 80 µm^2 maps, does not experience any relevant variation for F ≥ 0.86 J/cm^2, A_{ma} increases demonstrating further coalescence of surface features at high fluence. A jump in A_{ma} would be expected at the onset of coalescence, which is not evident in Fig. 6a also because of the relatively large error bars, determined as the standard deviation of A_{ma} over a set of topographic maps. In other words, S_{pd} and A_{ma} turn out not adequate to fully characterize the coalescence, since S_{pd} lacks in sensitivity in following the growth of surface features at high fluence and A_{ma} in detecting the process onset.

Figure 7b reports the motif mean slope (S_{ks}) as a function of the laser fluence. This dimensionless parameter is defined as [39]

$$S_{ks} = \frac{1}{N}\sum_{i}^{N}\frac{M_i}{2h_i} \quad (1)$$

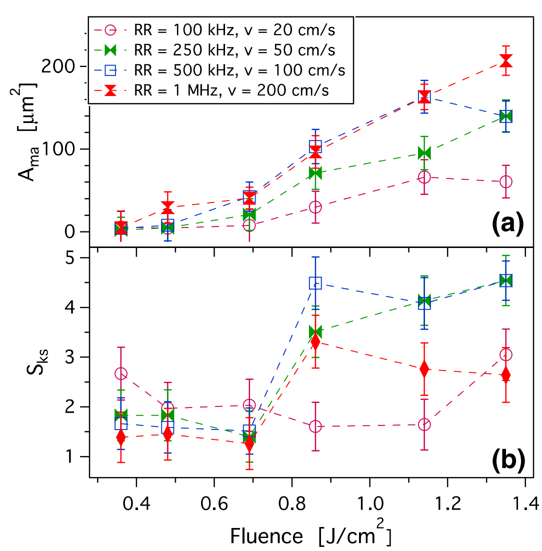

Fig. 7 Average motif area A_{ma} (**a**) and average motif slope S_{ks} (**b**) as a function of the laser fluence for different combinations of RR and v, as in legend. Data are evaluated analyzing different 80 × 80 µm^2 topographic maps; standard deviation is used for error bars. Dashed lines are guides for the eye

where N is the total number of motifs segmented by the watershed algorithm, h_i is the height and M_i the so-called equivalent diameter of the i-th motif:

$$M_i = \sqrt{\frac{4A_i}{\pi}} \tag{2}$$

with A_i area of the i-th motif.

According to this definition, an increase in S_{ks} implies a decrease in the average aspect ratio of surface features. The plot in Fig. 7b shows a jump at F > 0.69 J/cm^2 for all RR, with the exception of RR = 100 kHz. We can therefore conclude that the growth in transverse size of surface features at moderate fluence occurs at the expenses of their height, leading to a marked reduction of the aspect ratio. Furthermore, at high F S_{ks} maintains an almost constant value within error bars, again with the exception of RR = 100 kHz.

3.4 Role of Repetition Rate

The use of high repetition rate enhances process throughput as required for large-scale machining. The specific role of this parameter in determining island morphology must be clarified.

Figure 8 shows ShFM topographic maps of samples machined with the four choices of RR and v employed in the present work and F = 0.69 J/cm^2, a moderate fluence found to create bumps at RR = 500 kHz, as previously discussed in reference to Fig. 4. At fixed fluence and decreasing RR, a transition from bumps [see panels (a) and (b)] to small sized islands [panel (d)], similar to those produced at low F, can be seen.

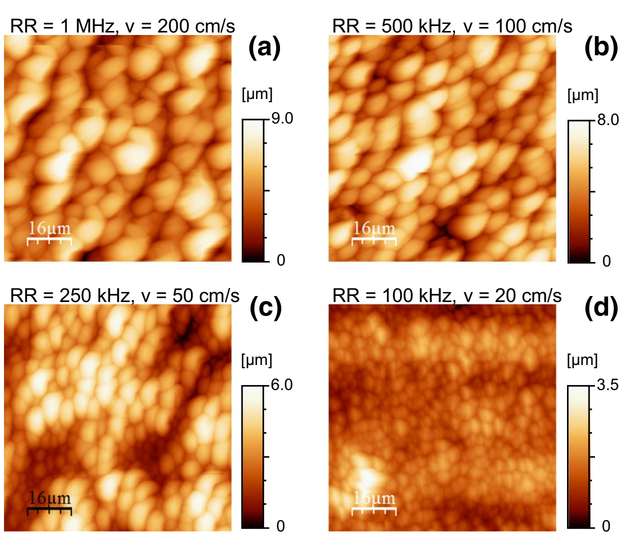

Fig. 8 80 × 80 μm^2 topographic maps of samples processed at F = 0.69 J/cm^2 and various combinations of RR and v (**a**)–(**d**)

We remark that the adopted scanning strategy enables constant displacement of the laser spot independent of repetition rate. Therefore, the morphological changes observed with changing RR must be related to this parameter only, i.e., the time interval Δt = 1/RR between subsequent pulses, which in the present experiment ranges from 1 μs to 1 ms. Several phenomena can be affected by Δt, including heat accumulation effects [40, 41]. The well-established two-temperature model [15] shows that phase transformation and material ejection following ultrashort pulsed laser irradiation are expected to produce a negligible HAZ due to the extremely short time-scale involved. In the case of metals, the HAZ is confined to within a few micrometers around the irradiated region [42]. Nonetheless, repetitive pulsed irradiation with high spatial overlap can result in a local increase in temperature due to heat accumulation. Such an increase depends on thermal conduction into the bulk material, with a low Δt leading to faster energy deposition and higher average temperatures.

The combined consequences of ablation and heat accumulated are cumbersome to be predicted because of the simultaneous occurrence of structural, chemical and surface modifications. Such a diverse set of effects, however, can be expected to result in overall features not much unlike those resulting from the well-known incubation effect [43, 44]. In practical terms, incubation leads to reduce the effective ablation threshold fluence depending on the number of previous shots fired in the same region [45]. We can therefore assume that an increase in RR enhances incubation effects due to heat accumulation. This leads, in turn, to a more effective use of the energy delivered by laser pulses in terms of material removal. It is therefore not surprising that a decrease in RR plays a qualitatively similar role to a decrease in F. It should be noted, however, that non-trivial interplay between ablation and redeposition does not lead to an obvious change in ablation depth under these conditions (see Fig. 2).

In principle, repetition rate could also be relevant in relation to expansion of the ablation plume during pulsed laser irradiation. Material removal can be described as a neutral and ionized ablation plume strongly oriented normal to the surface [46]. Plume expansion, governed by a complicated set of dynamics, takes place in a finite time depending on the process parameters and, in particular, the ambient gas pressure. The plume front has been shown to move several millimeters above the target surface in one microsecond following fs-laser ablation of an iron target in the presence of 50 mbar ambient gas [47]. In the present experiment, ablation is carried out in air, expected to further quench plume expansion and slow down its dynamics. We can infer that for Δt ≤ 2 μs, corresponding to RR ≥ 500 kHz, laser pulses interact with a relatively dense plume produced by preceding pulses. As a consequence, pulse energy is partially absorbed by the plume and the effective fluence arriving at the solid surface decreases. On the other hand, the resulting increase in electron temperature within the plume might contribute to modifying ablation features, e.g., by enhancing self-assembly mechanisms possibly involved in the transition from small islands to large bumps.

4 Conclusions

We have found that surface morphology of our machined samples depends strongly on the process parameters. Further to LIPSS, known to occur in ultra-short puled laser ablation of metals with linearly polarized light, a dense texture of surface features, denoted here as islands, is formed on AISI 316L stainless-steel as a consequence of repetitive laser irradiation. Thanks to the accurate three-dimensional topographic reconstruction enabled by ShFM, we were able to follow the evolution of the island morphology, from small features to relatively large bumps, as a function of laser fluence. Analysis of several selected areal surface parameters calculated over the whole set of processed samples allows us identifying the onset of transition between different morphological regimes at F ~ 0.69 J/cm^2. At such a value of laser fluence, small islands start merging each other. At the same time, their aspect ratio takes on values above 0.7, in general agreement with micro-conical spikes already reported in the literature. We interpret our results as a signature of a coalescence process involving neighboring small islands, which further proceeds at high fluence eventually leading to bumps with area in the order of hundreds μm^2. In such a process, growth in transverse size occurs faster than in height, leading to a decrease in the aspect ratio.

Results are of interest to devising practical strategies aimed at tailored surface patterning, for instance in the field of biomimetic surfaces where specifically shaped features must be produced. In particular, realization of anti-bio-film patterns can take advantage of the precise control over transverse size and height of produced features enabled by laser fluence.

Within this context, we obtained a relevant finding regarding the application of laser sources with high repetition rate, up to 1 MHz. Thanks to the use of a specifically conceived laser scanning strategy where spatial overlap of the laser spot was independent of the repetition rate, we were able to isolate the role played by this last parameter and found that an increase in RR leads to results qualitatively similar to an increase in F.

Acknowledgements This work has received funding from the EU Horizon 2020 Research and Innovation Programme under Grant Agreement No. 687613 "TresClean". GL, MA and FF gratefully acknowledge technical assistance with the ShFM setup from Nicola Puccini and Enrico Andreoni.

References

1. Pauleau, Y. (Ed.). (2006). *Materials surface processing by directed energy techniques—European materials research society series*. Amsterdam: Elsevier.
2. Bhushan, B. (2009). Biomimetics: lessons from nature—An overview. *Philosophical Transactions of the Royal Society A, 367,* 1445–1486.
3. Bhushan, B. (2016). *Biomimetics: bioinspired hierarchical-structured surfaces for green science and technology*. Berlin: Springer.
4. Yao, X., Song, Y., & Jiang, L. (2011). Applications of bio-inspired special wettable surfaces. *Advanced Materials, 23,* 719–734.
5. Kwon, M. H., Jee, W. Y., & Chu, C. N. (2015). Fabrication of hydrophobic surfaces using copper electrodeposition and oxidation. *International Journal of Precision Engineering and Manufacturing, 16,* 877–882.
6. Katsikogianni, M., & Missirlis, Y. F. (2004). Concise review of mechanisms of bacterial adhesion to biomaterials and of techniques used in estimating bacteria-material interactions. *European Cells & Materials, 8,* 37–57.
7. Lutey, A. H., Gemini, L., Romoli, L., Lazzini, G., Fuso, F., Faucon, M., et al. (2018). Towards laser-textured antibacterial surfaces. *Scientific Reports, 8,* 1–10.
8. Wu, D., Wang, J., Wu, S., Chen, Q., Zhao, S., Zhang, H., et al. (2011). Three-level biomimetic rice-leaf surfaces with controllable anisotropic sliding. *Advanced Functional Materials, 21,* 2927–2932.
9. Ko, D., Tumbleston, J. R., Henderson, K. J., Euliss, L. E., De Simone, J. M., Lopez, R., et al. (2011). Biomimetic microlens array with antireflective moth-eye surface. *Soft Matter, 7,* 6404–6407.
10. Lee, H., Lee, P. B., & Messersmith, P. B. (2007). A reversible wet/dry adhesive inspired by mussels and geckos. *Nature, 448,* 338–341.
11. Feng, J., Tuominen, M. T., & Rothstein, J. P. (2011). Hierarchical superhydrophobic surfaces fabricated by dual-scale electron-beam-lithography with well-ordered secondary nanostructures. *Advanced Functional Materials, 21,* 3715–3722.
12. Valbusa, U., Boragno, C., & Buatier de Mongeot, F. (2002). Nanostructuring surfaces by ion sputtering. *Journal of Physics: Condensed Matter, 14,* 8153–8175.
13. D'Acunto, M., Fuso, F., Micheletto, R., Naruse, M., Tantussi, F., & Allegrini, M. (2017). Near-field surface plasmon field enhancement induced by rippled surfaces. *Beilstein Journal of Nanotechnology, 8,* 956–967.
14. Lee, C. M., Woo, W. S., Baek, J. T., & Kim, E. J. (2016). Laser and arc manufacturing processes: A review. *International Journal of Precision Engineering and Manufacturing, 17,* 973–985.
15. Chichkov, B. N., Momma, C., Nolte, S., von Alvensleben, F., & Tünnermann, A. (1996). Femtosecond, picosecond and nanosecond laser ablation of solids. *Applied Physics A, 63,* 109–115.
16. Bonse, J., Hohm, S., Kimer, S. V., Rosenfeld, A., & Kruger, J. (2017). Laser-induced periodic surface structures—A scientific evergreen. *IEEE Journal of Selected Topics in Quantum Electronics, 23,* 9000615.
17. Reif, J., Varlamova, O., Uhlig, S., Varlamov, S., & Bestehorn, M. (2014). On the physics of self-organized nanostructure formation upon femtosecond laser ablation. *Applied Physics A, 117,* 179–184.
18. Lazzini, G., Romoli, L., Blunt, L., & Gemini, L. (2017). Design and characterization of textured surfaces for applications in the

food industry. *Surface Topography: Metrology and Properties, 5,* 044005.
19. Tantussi, F., Vella, D., Allegrini, M., Fuso, F., Romoli, L., & Rashed, C. A. A. (2015). Shear-force microscopy investigation of roughness and shape of micro-fabricated holes. *Precision Engineering, 41,* 32–39.
20. Romoli, L., Rashed, C. A. A., Lovicu, G., Dini, G., Tantussi, F., Fuso, F., et al. (2014). Ultrashort pulsed laser drilling and surface structuring of microholes in stainless steels. *CIRP Annals-Manufacturing Technology, 63,* 229–232.
21. Rashed, C. A. A., Romoli, L., Tantussi, F., Fuso, F., Bertoncini, L., Fiaschi, M., et al. (2014). Experimental optimization of micro-electrical discharge drilling process from the perspective of inner surface enhancement measured by shear-force microscopy. *CIRP Journal of Manufacturing Science and Technology, 7,* 11–19.
22. Karrai, K., & Tiemann, I. (2000). Interfacial shear force microscopy. *Physical Review B, 62,* 13174–13181.
23. Pietroy, D., Di Maio, Y., Moine, B., Baubeau, E., & Audouard, E. (2012). Femtosecond laser volume ablation rate and threshold measurements by differential weighing. *Optics Express, 20,* 29900–29908.
24. Momma, C., Chichkov, B. N., Nolte, S., von Alvensleben, F., Tünnermann, A., Welling, H., et al. (1996). Short-pulse laser ablation of solid targets. *Optics Communication, 129,* 132–134.
25. Nečas, D., & Klapetek, P. (2012). Gwyddion: An open-source software for SPM data analysis. *Central European Journal of Physics, 10,* 181–188.
26. Sipe, J. E., Young, J. F., Preston, J. S., & van Driel, H. M. (1983). Laser-induced periodic surface structure. I. Theory. *Physical Review B, 27,* 1141–1154.
27. Young, J. F., Preston, J. S., van Driel, H. M., & Sipe, J. E. (1983). Laser-induced periodic surface structure. II. Experiments on Ge, Si, Al, and brass. *Physical Review B, 27,* 1155–1172.
28. Bonse, J., Hohm, S., Kimer, S. V., Rosenfeld, A., & Kruger, J. (2012). Femtosecond laser-induced periodic surface structures. *Journal of Laser Applications, 24,* 042006.
29. Pham, K. X., Tanabe, R., & Ito, Y. (2013). Laser-induced periodic surface structures formed on the sidewalls of microholes trepanned by a femtosecond laser. *Applied Physics A, 112,* 485–493.
30. Lazzini, G., Romoli, L., Tantussi, F., & Fuso, F. (2018). Nanostructure patterns on stainless-steel upon ultrafast laser ablation with circular polarization. *Optics & Laser Technology, 107,* 435–442.
31. Gemini, L., Hashida, M., Shimizu, M., Miyazaka, Y., Inoue, S., Tokita, S., et al. (2013). Metal-like self-organization of periodic nanostructures on silicon and silicon carbide under femtosecond laser pulses. *Journal of Applied Physics, 114,* 194903.
32. Martinez-Calderon, M., Rodriguez, A., Dias-Ponte, A., Morant-Miñana, M. C., Gomez-Aranzadi, M., & Olaizola, S. M. (2016). Femtosecond laser fabrication of highly hydrophobic stainless steel surface with hierarchical structures fabricated by combining ordered microstructures and LIPSS. *Applied Surface Science, 374,* 81–89.
33. Mincuzzi, G., Gemini, L., Faucon, M., & Kling, R. (2016). Extending ultra-short pulse laser texturing over large area. *Applied Surface Science, 386,* 65–71.
34. Choi, S. H., Sohn, I. B., & Lee, H. (2012). Femtosecond laser-induced line structuring on mold stainless steel STAVAX with various scanning speeds and two polarization configurations. *International Journal of Precision Engineering and Manufacturing, 13,* 845–854.
35. Kam, D. H., Bhattacharya, S., & Mazumder, J. (2012). Control of the wetting properties of an AISI 316L stainless steel surface by femtosecond laser-induced surface modification. *Journal of Micromechanics and Microengineering, 22,* 105019.
36. Nayak, B. K., Gupta, M. C., & Kolasinski, K. W. (2008). Formation of nano-textured conical microstructures in titanium metal surface by femtosecond laser irradiation. *Applied Physics A, 90,* 399–402.
37. Nayak, B. K., & Gupta, M. C. (2010). Self-organized micro/nano structures in metal surfaces by ultrafast laser irradiation. *Optics and Lasers in Engineering, 48,* 940–949.
38. Tsibidis, G. D., Fotakis, C., & Stratakis, E. (2015). From ripples to spikes: A hydrodynamical mechanism to interpret femtosecond laser-induced self-assembled structures. *Physical Review B, 92,* 041405(R).
39. Leach, R. (2013). Introduction to surface topography. In *Characterisation of areal surface texture*. Springer.
40. Eaton, S. M., Zhang, H., Herman, P. R., Yoshino, F., Shah, L., Bovatsek, J., et al. (2005). Heat accumulation effects in femtosecond laser-written waveguides with variable repetition rate. *Optics Express, 13,* 4708–4716.
41. Marla, D., Barde, V., & Joshi, S. S. (2013). Analytical model to predict temperature distribution and ablation depth in excimer laser micromachining. *International Journal of Precision Engineering and Manufacturing, 14,* 29–36.
42. Le Harzic, R., Huot, N., Audouard, E., Jonin, C., Laporte, P., Valette, S., et al. (2002). Comparison of heat-affected zones due to nanosecond and femtosecond laser pulses using transmission electronic microscopy. *Applied Physics Letters, 80,* 3886–3888.
43. Di Niso, F., Gaudiuso, C., Sibillano, T., Mezzapesa, F. P., Ancona, A., & Lugarà, P. M. (2014). Role of heat accumulation on the incubation effect in multi-shot laser ablation of stainless steel at high repetition rates. *Optics Express, 22,* 12200–12210.
44. Di Niso, F., Gaudiuso, C., Sibillano, T., Mezzapesa, F. P., Ancona, A., & Lugarà, P. M. (2013). Influence of the repetition rate and pulse duration on the incubation effect in multiple-shots ultrafast laser ablation of steel. *Physics Procedia, 41,* 698–707.
45. Güdde, J., Hohlfeld, J., Müller, J. G., & Matthias, E. (1998). Damage threshold dependence on electron-phonon coupling in Au and Ni films. *Applied Surface Science, 127–129,* 40–45.
46. Anisimov, S. I., & Luk'yanchuk, B. S. (2002). Selected problems of laser ablation theory. *Physics-Uspekhi, 45,* 293–324.
47. Amoruso, S., Bruzzese, R., Wang, X., & Xia, J. (2008). Propagation of a femtosecond pulsed laser ablation plume into a background atmosphere. *Applied Physics Letters, 92,* 041503.

Publisher's Note Springer Nature remains neutral with regard to jurisdictional claims in published maps and institutional affiliations.

G. Lazzini PhD student in Physics at Università degli Studi di Parma, Italy. His research interests are surface physics and numerical modeling of the interaction between machined surfaces and biological cells.

L. Gemini Group Manager, Nanoscale Laser Processing at ALPhANOV, Bordeaux, France. Her main research interests are laser micromachining and nanoscale processing, and related applications.

A. H. A. Lutey Research Fellow (Ricercatore) at Università degli Studi di Parma, Italy. His main research interests are industrial applications of laser processing, including cutting, machining, ablation.

R. Kling Manager of Laser Micromachining Department at ALPhANOV, Bordeaux, France. His main research interests are laser micromachining and nanoscale processing, and related applications.

L. Romoli Associate Professor in Industrial Engineering at Università degli Studi di Parma, Italy. His main research interests are innovative laser technologies for the development of modern manufacturing processes.

M. Allegrini Full Professor in Physics of the Matter at Università di Pisa, Italy. Her main present research interests are scanning probe microscopy and nanotechnology.

F. Fuso Associate Professor in Physics of the Matter at Università di Pisa, Italy. His main present research interests are laser applications to nanotechnologies and advanced nanoscopies.